

Full length article

A combined kinetic Monte Carlo and phase field approach to model thermally activated dislocation motion

Xiaoyao Peng^{a,*}, Nithin Mathew^a, Irene J. Beyerlein^{b,c}, Enrique Martinez^{d,e,*}, Abigail Hunter^{f,*}

^a Theoretical Division, Los Alamos National Laboratory, United States of America

^b Department of Mechanical Engineering, University of California, Santa Barbara, United States of America

^c Materials Department, University of California, Santa Barbara, United States of America

^d Department of Mechanical Engineering, Clemson University, Clemson, United States of America

^e Department of Materials Science and Engineering, Clemson University, Clemson, United States of America

^f X Computational Physics Division, Los Alamos National Laboratory, United States of America

ARTICLE INFO

Keywords:

Phase field model

Kinetic Monte Carlo

Dislocations

Thermal activation

ABSTRACT

In this work, a kinetic Monte Carlo (KMC) scheme is integrated into a phase field dislocation dynamics (PFDD) model to account for thermal activation. While the implementation is general and could be applied to many different thermally activated processes, we apply the model to simulate a dislocation transmitting through an interface. Two cases are analyzed: a dislocation transmitting through a strong interface, and a dislocation transmitting through a more realistic grain boundary in tungsten. Results and trends for both cases are discussed in detail, and ultimately show that the combined KMC-PFDD algorithm is effective in capturing thermally activated dislocation processes.

1. Introduction

Many aspects of material deformation and development of microstructure are controlled by thermally activated processes. Mesoscale models of dislocation dynamics, such as phase field dislocation dynamics (PFDD) and discrete dislocation dynamics (DDD), were conventionally developed and applied in the athermal regime. In this regime, energetic barriers for dislocation motion are overcome only by application of high enough stresses. This especially limits the application of these methods at low strain rates and in materials with low lattice friction, as gliding dislocations remain pinned at obstacles, such as precipitates, point defect clusters, stacking fault tetrahedra (SFTs), interfaces, and dislocation junctions. One of the approaches proposed to overcome this limitation is to modify the equations of motion for dislocations using stochastic forces derived in the Langevin formalism. This approach has been applied in the DDD model, leading to the development of Stochastic Dislocation Dynamics (SDD) [1]. SDD has been applied to investigate dislocation-defect interactions [1], dislocation patterning [2], and recently to thermal diffusion of prismatic dislocation loops in body centered cubic (BCC) Fe [3]. An alternate approach is based on the well known kinetic Monte Carlo (KMC) scheme to simulate thermally activated processes. In this scheme, state-to-state dynamics of the system is followed using rate coefficients for unit processes, which are typically inferred from atomic-scale simulations or experiments.

The KMC method has been applied to study thermally activated glide of screw dislocations in BCC metals [4–6], shear-coupled motion of grain boundaries [7], and dislocation motion in alloys [8–11].

Phase field approaches, including PFDD [12] and several others [13, 14], targeting dislocation dynamics have been under development now for several decades. These approaches track the evolution and interactions of individual dislocations and rely on energy minimization to evolve the dislocation configuration. While these approaches have been applied to a wide range of material systems [15–20] and problems [21–23], very few have considered the effect of temperature, minimizing only to the athermal energy minimum. In cases where temperature dependence has been considered, a Langevin noise term is added to simulate thermal fluctuations in the material [13,24,25]. This approach is similar to Langevin noise terms used more traditionally in phase field approaches addressing phase transformation to account for nucleation [26,27].

In this paper, we introduce the KMC-PFDD method for modeling thermally activated processes in dislocation-mediated plasticity. This paper is organized as follows: Section 2 presents a brief summary of the PFDD method. Integration of the KMC algorithm with the PFDD method is described in Section 3. Results and related discussion addressing the slip transfer of a dislocation through two different types of interfaces are presented in Section 4. Finally, the work is summarized in Section 5.

* Corresponding authors.

E-mail addresses: jpeng@lanl.gov (X. Peng), enrique@clemson.edu (E. Martinez), ahunter@lanl.gov (A. Hunter).

<https://doi.org/10.1016/j.commatsci.2023.112490>

Received 19 June 2023; Received in revised form 31 August 2023; Accepted 2 September 2023

Available online 18 September 2023

0927-0256/© 2023 Elsevier B.V. All rights reserved.

2. Summary of phase field dislocation dynamics (PFDD)

In the PFDD formulation, dislocations and their motion are tracked using scalar-valued order parameters $\zeta^\alpha(X, t)$ defined on each active slip system α such that integer values represent perfect Burgers vector translations, i.e., where the crystal has undergone slip, zero-value order parameters imply no slip, and non-integer order parameters indicate the location of the dislocation core, where the atoms in the crystal structure are distorted and not perfectly aligned. The plastic strain due to dislocation motion, $\epsilon^p(X, t)$, can be expressed as a function of the order parameters via:

$$\epsilon^p(X, t) = \frac{1}{2} \sum_{\alpha=1}^N \frac{b^\alpha}{d^\alpha} \zeta^\alpha(X, t) (s^\alpha \otimes m^\alpha + m^\alpha \otimes s^\alpha), \quad (2.1)$$

where N is the number of active slip systems, b^α is the magnitude of the Burgers vector b^α , s^α is the normalized Burgers vector, m^α is the slip plane normal, and d^α is the interplanar spacing between slip planes.

The order parameters evolve in time using a time-dependent Ginzburg–Landau (TDGL) kinetic equation, which minimizes the total system energy $E(\zeta)$ and allows for stress equilibrium $\nabla \cdot \sigma = 0$:

$$\frac{\partial \zeta^\alpha(X, t)}{\partial t} = -L \frac{\partial E(\zeta^\alpha)}{\partial \zeta^\alpha(X, t)} \quad (2.2)$$

where the coefficient L has been traditionally utilized as a relaxation coefficient that governs the rate at which the system converges to the 0 K athermal equilibrium [28,29]. With the implementation of the KMC algorithm within PFDD, this coefficient is, in part, informed with the material's drag coefficient. This is discussed in more detail later in Section 3.3.

The total system energy comprises three terms in the model discussed here, namely the elastic strain energy, E^{strain} , the lattice energy, $E^{lattice}$, and the external energy, E^{ext} . It is also possible to include other terms in the energy functional, such as a gradient energy term [30,31]; however, this term is not utilized in the current work. The elastic strain energy includes dislocation–dislocation interactions, while the external energy represents dislocation interactions with the applied stress state. The lattice energy describes the energy required to break and reform atomic bonds as a dislocation moves through the crystal, and thus is dependent upon the material system and glide plane being modeled. Below are the expressions for each energy term.

$$E^{strain} = \frac{1}{2} \int C_{ijkl} \epsilon_{ij}^e(X, t) \epsilon_{kl}^e(X, t) d^3 X \quad (2.3)$$

$$E^{ext} = \int \sigma_{ij}^{app} \epsilon_{ij}^p d^3 X \quad (2.4)$$

$$E^{lattice} = \sum_{\alpha=1}^N \int B_0 \beta(\theta^\alpha(X, t)) (\sin n \pi \zeta^\alpha(X, t))^2 \delta_\alpha d^3 X, \quad (2.5)$$

where $\epsilon^e = \epsilon - \epsilon^p$. Once this relation is applied, $E^{strain}(\zeta)$ of Eq. (2.3) can be transformed into Fourier space under the stress equilibrium condition, which gives a functional form that is directly related to ϵ^p and thus, the order parameter, ζ [32]. C is the stiffness tensor, and σ^{app} is the applied stress. The occurrence of indices in pairs indicates Einstein summation convention.

In the lattice energy term, B_0 is the magnitude of the energy barrier to activate slip, and δ_α is a Dirac distribution supported on the slip plane of slip system α . The transition function $\beta(\theta)$ is given by

$$\beta(\theta) = (1 - \frac{1}{R}) \cos^2 \theta + \frac{1}{R} \quad (2.6)$$

where θ is the line character angle, and $R = \frac{\sigma_{screw}}{\sigma_{edge}}$ is the ratio of the

Peierls stress for screw to edge. This transition function accounts for dislocation character dependence within the lattice energy term, and has been proposed previously [18]. In essence, this term accounts for differences in Peierls barriers between screw, edge, and mixed type dislocations in BCC materials. While it is well-known that these differences are a consequence of the non-planar core structure of screw dislocations

versus the planar core of the edge dislocation, the PFDD methodology presented here does not explicitly capture these differences. Rather we capture the effect of the different core structures on the evolution of the dislocations through modification of the lattice energy with the transition function. The lattice energy presented has been used in previous efforts to describe the motion of perfect dislocation in BCC materials [16,33]. In [16], another functional form of the transition function was used and had been informed with atomistic data. For the case here, the needed atomistic data is not available, and therefore, we utilize Eq. (2.6). We note that a very recent work [33] has extended PFDD to capture the different core structures between screw and edge-type dislocations in BCC materials, obviating the need for the transition function.

3. Incorporation of Kinetic Monte Carlo (KMC)

The original PFDD method and all previous applications assumed 0 K temperature; therefore, the energy minima reached in previous studies were athermal; i.e., those accessible to the system without thermal activation. In this work, we incorporate a KMC algorithm to enable thermal activation in PFDD through the first-reaction method [34], such that the system will be able to overcome energetic barriers with thermal energy. To the best of the authors' knowledge, this is the first time in which a phase field model and the KMC algorithm have been integrated for the study of thermally activated dislocation behavior.

3.1. First reaction method

The first-reaction method gives the event time that is required for a given event to happen. The only input for the KMC routine is the event rate Γ_k , with which the event time of event k can be calculated as:

$$\Delta t_k = \frac{1}{\Gamma_k} \ln\left(\frac{1}{r_k}\right) \quad (3.1)$$

where r_k is a random number from the uniform distribution in the unit interval. When Δt_k is generated this way it satisfies the exponential distribution $P(\Delta t_k) = \Gamma_k \exp(-\Gamma_k \Delta t_k)$ [34]. In this work, the event rate is determined through [35]:

$$\Gamma_k = v_{eff} \exp(-\Delta H(\sigma)/\kappa_b T) \quad (3.2)$$

$$\Delta H(\sigma) = \Delta E_0 - V_{ij} \sigma_{ij}^{app} \quad (3.3)$$

where v_{eff} is a pre-factor, κ_b is Boltzmann's constant, T is the absolute temperature, ΔE_0 is the activation energy and V_{ij} is the activation volume. We note here that for this work we utilized the applied or global stress state σ_{ij}^{app} in this equation. An alternate approach would be to consider the local stress state at each different dislocation segment, which then could evolve and change the energy barrier based on dislocation segment motion and interaction. This may be necessary to capture certain phenomena, however we leave this extension for future work.

The KMC routine was embedded in the PFDD algorithm to enable on-the-fly calculations according to the flowchart in Fig. 1, where Δt_k ($k = 1, 2, 3, \dots$) is the event time sampled according to Eq. (3.1) and Δt is the PFDD time step. At every PFDD iteration step, each grid point within the computational cell will undergo the steps shown in the flowchart. Initially, the system proceeds through the original PFDD energy minimization as described in Section 2. During each time step, the KMC routine will evaluate if any events have been triggered by checking if the dislocation reaches a pre-defined configuration. If one event is triggered (i.e., if an event is triggered at any computational grid point), PFDD evolution is paused at this point (i.e., $\zeta(X(i, j, k))$ will not be updated during this iteration step), and event times will be sampled and sorted for all triggered events. The smallest of them, Δt_1 , corresponds to the event that will happen first. If Δt_1 is less than Δt , meaning the event will happen before the start of next PFDD iteration, the PFDD evolution will restart and the order parameter will evolve

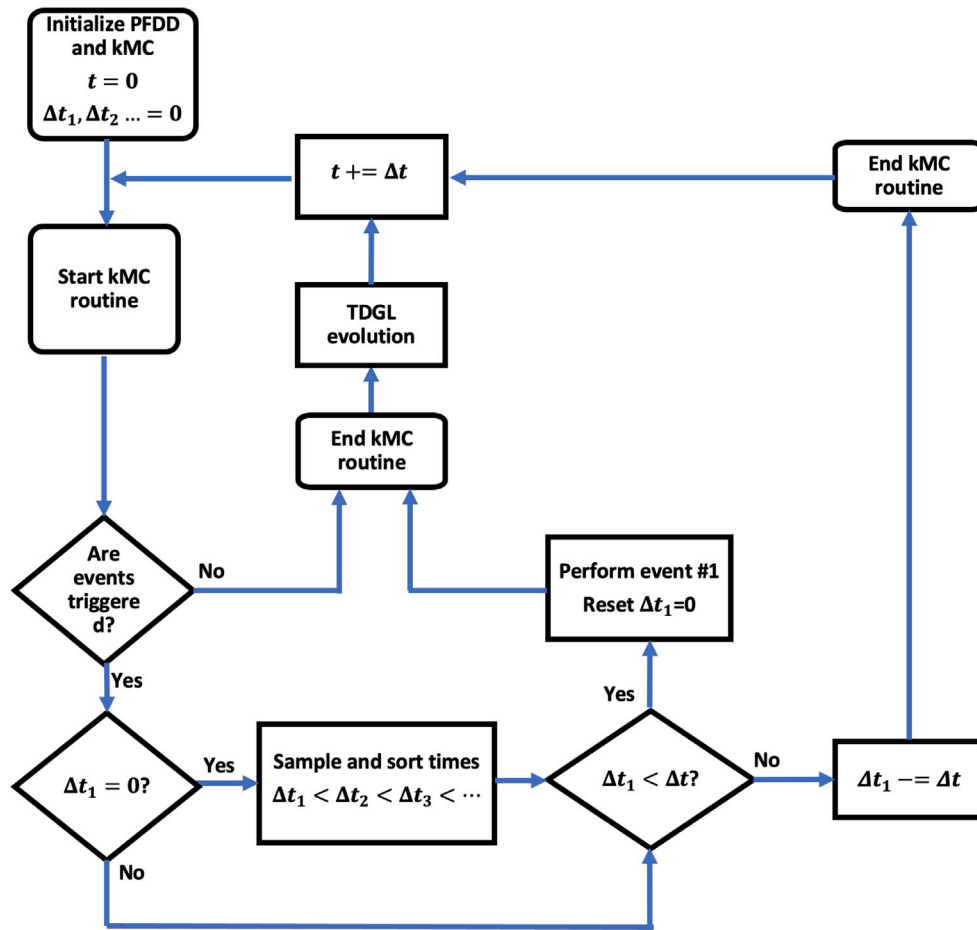


Fig. 1. Flowchart showing how the KMC routine was incorporated into the PFDD algorithm.

following the system of equations described in Section 2. Generally, this will result in the event of interest occurring. However, unlike a conventional KMC simulation where the ‘event’ is performed, the order parameter in PFDD itself is not perturbed in any way by the KMC algorithm after a segment has waited Δt . Instead, we simply let the segment evolve as determined by the energy equations of the standard PFDD approach. Thus, any motion of the order parameter is guided by the energy evolution equations for the standard PFDD approach. In some cases, when the evolution at a grid point restarts, it could take a few more iteration steps for the event to complete. During that time, the condition that can trigger a new event may still hold. Therefore, we only allow the evolution at a grid point to trigger a new KMC event after the completion of the previous one. This is done by monitoring the value of the second-order directional derivative of the order parameter along the gradient direction, the details of which are discussed in Section 3.2.

If Δt is not longer than the event time determined for a given point, TDGL evolution will continue to be paused and Δt_1 will be updated as $\Delta t_1 = \Delta t_1 - \Delta t$ after each PFDD iteration. In other words, the order parameter values (or the dislocations) will “wait” in the current configuration until the event time has lapsed. Thus, event 1 will be performed after $\text{int}(\Delta t / \Delta t_1)$ number of PFDD iterations.

As integrated, it is in principle possible to solve all aspects of the dislocation motion using KMC, including fluctuations back and forth assuming rates (or energy barriers) to inform the model are available for these processes. Conceptually, the KMC-PFDD framework would treat ‘forward’ and ‘backward’ hops separately so that the activation energy is always calculated as the difference between the initial state (defined separately for forward and backward hops) and the saddle point. Such

an approach would be extremely time consuming, thus our focus is on thermally activated dislocation processes that occur on longer time scales. It is worth noting that the effects of temperature on interfaces and dislocation motion have been modeled at much finer time and length scales, where thermal fluctuations from Brownian motion are relevant, using Langevin dynamics [25,36]. This type of formulation, however, cannot follow dislocation trajectories across hard obstacles, with long wait times.

3.2. Precise determination of the center of a dislocation

Since the primary focus of the new KMC-PFDD code is to model the motion and interaction of dislocations, all thermally activated events of interest for study will depend on the location of the dislocations at any given time during a simulation. Thus, to evaluate if relevant events are triggered at each grid point, we need to determine the location of each dislocation. Previous works of PFDD treated the dislocation core region as the location of the dislocation [37]. This region is generally defined as the non-integer transition region in an order parameter, for example the smooth transition from 0 to 1. Thus, the core region has a width of δ , making it so that the location of the dislocation is spread over a region. The region is too broad, such that an additional criterion is needed to determine the location of the dislocation and thus, whether or not its location has triggered an event. In this work, we chose the inflection points of the order parameter field along the gradient direction as the “dislocation center”, and treated it as the location of the dislocation. Fig. 2 shows the order parameter of a dislocation along the gradient direction, and the inflection point is the point X that:

$$\zeta''(X) = 0 \quad (3.4)$$

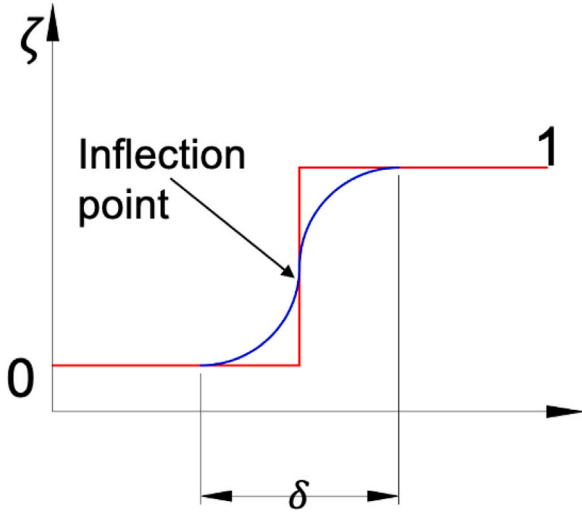


Fig. 2. Order parameter along its gradient direction. The red curve shows this initial condition for a single dislocation, which is typically set as a step function. As the system evolves, the dislocation core region will relax to have a smooth transition and core width, as illustrated with the blue curve.

$$\zeta''(X + \Delta X)\zeta''(X - \Delta X) < 0 \quad (3.5)$$

where ΔX represents a small step along the gradient direction.

In 3D, Eqs. (3.4) and (3.5) correspond to:

$$\zeta_n''(X) = 0 \quad (3.6)$$

$$\zeta_n''(X + \Delta X)\zeta_n''(X - \Delta X) < 0 \quad (3.7)$$

where \mathbf{n} is the gradient $\nabla\zeta$, and $\zeta_n''(X)$ is the second-order directional derivative of the order parameter along the gradient direction, which can be calculated with:

$$\zeta_n''(X) = \mathbf{n} \cdot \mathbf{H}(X)\mathbf{n} \quad (3.8)$$

where $\mathbf{H}(X)$ is the Hessian matrix of the order parameter at X . Grid points satisfying Eqs. (3.6) and (3.7) will be selected as the dislocation center. Additional details about how these criteria are executed and inflection points are selected are included in the Appendix. This dislocation center can be tracked throughout the KMC-PFDD simulations, and used to determine if specific dislocation configurations occur, such that an event of interest has happened and the KMC algorithm should be triggered. This is illustrated in Fig. 3, for an example case of a perfect dislocation loop expanding in a BCC material. The transition region of the single active order parameter is plotted (i.e., grid points with non-integer values of the order parameter), with the inflection points marked in red. The core is fairly narrow in this case. However, the figure shows that a subset of the grid points with non-integer order parameter values are selected as the dislocation “center” and can be tracked during dislocation evolution. We note that this calculation does require the computational grid spacing to be sufficiently resolved to capture the dislocation core width region.

Furthermore, we highlight that the dislocation center is often indicated with two points along the dislocation line thickness. This is subjected to parameters used in the selecting criteria. In Fig. 3, segments at the top and bottom are more likely to have two points selected, whereas segments at the diagonal tends to have only one point. In this work, we chose parameters such that the selected points can form a closed loop. In cases where the dislocation center is identified with more than one point, when the leading point (where the inflection point is the point that triggers the KMC algorithm first) reaches a specific configuration, the KMC algorithm will be triggered. Once the appropriate wait time has passed, the event will be performed and the leading point will continue within the TDGL evolution. While the trailing point

Table 1

Transformation rules between the cubic and the non-orthogonal grid.

Type	Cubic	Non-orthogonal
Coordinates	X_i	$F_{ij}x_j$
Gradient $\nabla\zeta$	$\frac{\partial\zeta}{\partial X_i}$	$F_{ij}^{-T} \frac{\partial\zeta}{\partial x_j}$
Hessian \mathbf{H}	$\frac{\partial^2\zeta}{\partial X_i\partial X_j}$	$F_{ik}^{-T} \frac{\partial^2\zeta}{\partial x_k\partial x_m} F_{mj}^{-1}$

has the potential to re-trigger the KMC algorithm, this is not allowed as discussed previously in Section 3.1. The entire dislocation center region, as defined by the Hessian calculation will continue within the PFDD evolution.

In previous work [32], non-orthogonal computational grids were implemented in PFDD and were shown to reduce numerical errors. When using a non-orthogonal grid, where the dislocation network is initially assigned and evolves, all calculations are still performed on the global (cubic) grid. To conduct the Hessian calculation with use of a local non-orthogonal grid, we added a transformation from the local (non-orthogonal) grid to the global (cubic) grid.

A point $\mathbf{r} \in \mathbb{R}^3$ can be represented in the cubic grid as $\mathbf{X}(\mathbf{r}) = (i, j, k)$ and in the non-orthogonal grid as $\mathbf{x}(\mathbf{r}) = (l, m, n)$.

$$\mathbf{r} = i \times \mathbf{e}_1^o + j \times \mathbf{e}_2^o + k \times \mathbf{e}_3^o = l \times \mathbf{p}_1 + m \times \mathbf{p}_2 + n \times \mathbf{p}_3 \quad (3.9)$$

where $\{\mathbf{e}_i^o\}$ is the basis of the cubic grid, i.e. $\mathbf{e}_1^o = [1, 0, 0]^T$, $\mathbf{e}_2^o = [0, 1, 0]^T$, $\mathbf{e}_3^o = [0, 0, 1]^T$; $\{\mathbf{p}_i\}$ is the basis of the non-orthogonal grid, and $\{\mathbf{p}_1\} = \frac{1}{\sqrt{3}}[111]^T$, $\{\mathbf{p}_2\} = \frac{1}{\sqrt{3}}[1\bar{1}1]^T$, $\{\mathbf{p}_3\} = \frac{1}{\sqrt{3}}[11\bar{1}]^T$ for BCC. The transformation matrix between the two grids is $\mathbf{F} = [\mathbf{p}_1|\mathbf{p}_2|\mathbf{p}_3]$ and

$$\mathbf{x} = \mathbf{F}^{-1}\mathbf{X} \quad (3.10)$$

We summarized all the transformations between the cubic and non-orthogonal grids in Table 1.

3.3. Calibration of PFDD time step

One of the important steps in the KMC routine is to determine if $\Delta t_1 < \Delta t$. While Δt_1 can be calculated with Eq. (3.1), the PFDD time step Δt depends on the coefficient L and can be adjusted according to the mesh resolution [13,38]. In the PFDD algorithm, each iteration follows Eq. (2.2) and evolution is performed explicitly with:

$$\zeta^\alpha(\mathbf{X}, t + \Delta t) = \zeta^\alpha(\mathbf{X}, t) - \Delta t L \frac{\partial E(\zeta)}{\partial \zeta^\alpha(\mathbf{X}, t)} \quad (3.11)$$

where Δt is coupled with L as $\Delta t L = \frac{c}{\mu}$ (c is a constant and μ is the shear modulus) such that Eq. (2.2) is non-dimensional. It is common practice in phase field approaches for calculations to be performed using non-dimensional equations [13,38]. However, in order to compare to the KMC time, a physical time scale is required. To achieve this, Δt and L must be decoupled.

We use simulations of a gliding screw dislocation in a representative BCC metal to calibrate the PFDD time step. In [39], a two-regime mobility law was developed for dislocations in BCC metals, where the relation between the velocity and the drag coefficient B in the phonon-drag regime was written as:

$$v = \frac{\tau b}{B(T)} \quad (3.12)$$

where τ is the resolved shear stress. To decouple Δt and L , we set-up a series of simulations of a W (tungsten) screw dipole gliding under the same temperature but different values of resolved shear stress. The simulations were performed in the non-orthogonal BCC grid with a grid spacing of $b:b:b$ and grid size of $64b \times 64b \times 64b$. For all calculations that follow, we used anisotropic elasticity with the material parameters for W listed in Table 2. These parameters were obtained using molecular dynamics/statics (MD/MS) calculations using the EAM2 potential in Ref. [40], which predicts the non-degenerate core structure for screw

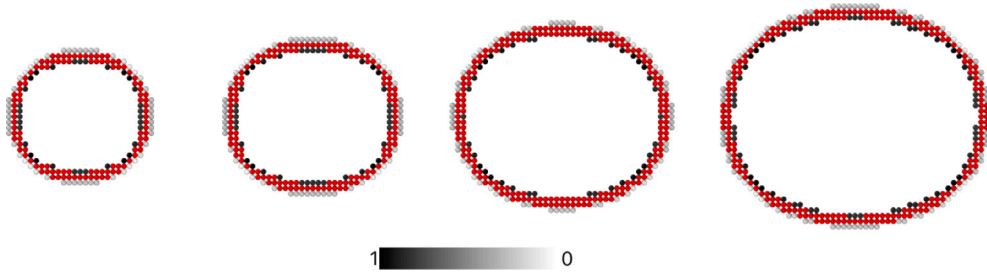


Fig. 3. Snapshots of a dislocation loop expansion; the loop is colored by the value of the order parameter and the grid points selected to be the dislocation center by the Hessian calculation are marked in red. Order parameter values of one inside the loop are removed to better indicate the transition region of the order parameter.

Table 2

Material parameters for W. Isotropic elastic moduli (shear modulus μ and young's modulus E) were calculated using the Voigt average. All elastic coefficients are specified in units of GPa.

Material	Lattice parameter (Å)	C_{11}	C_{12}	C_{44}	μ	E	γ_U (mJ/m ²)	B (Pa s)
W	3.14	544	208	160	163.2	418.46	1505.7079	8.77×10^{-4}

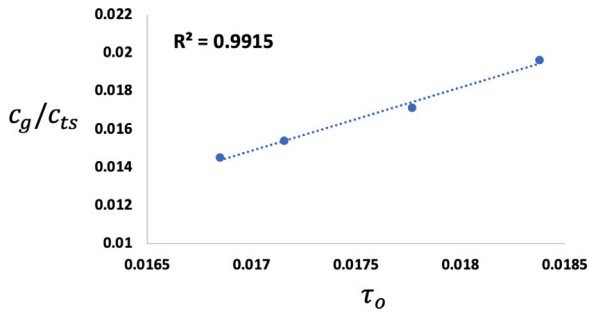


Fig. 4. Calculated normalized velocity as a function of normalized applied stress.

dislocations at 0 K. The value of B used in the PFDD simulations was extrapolated from data in Ref. [41]. We note that B was used as a constant, i.e., a functional dependence on temperature was not included.

Given that the applied stress, the drag coefficient, and the Burgers vector are known, we can calibrate the time step by measuring the distance the screw dislocation moves as a function of the applied stress. In the case that the dipole glides $c_g b$ (where c_g is the number of grid spaces in a mesh with the resolution of a Burgers vector magnitude in the glide direction) in c_{ts} iteration steps under resolved shear stress $\tau = \tau_o \mu$, the average velocity would be: $\bar{v} = \frac{c_g b}{c_{ts} \Delta t}$. Fig. 4 plots the results of these tests. Thus,

$$\frac{1}{B} = \frac{v}{\tau b} \approx \frac{\bar{v}}{\tau b} = \frac{c_g}{\tau_o c_{ts}} \frac{1}{\mu \Delta t} \quad (3.13)$$

the slope of the interpolation line in Fig. 4 provides an approximated value of $\frac{c_g}{\tau_o c_{ts}} \approx 3.32$. Therefore,

$$\Delta t = \frac{c_g}{\tau_o c_{ts}} \frac{B}{\mu} = 1.78 \times 10^{-14} \text{ s} \quad (3.14)$$

We note that $c = \frac{1}{2}$ for all the simulations in this work. Further, Δt can be adjusted by varying the c value as $\frac{c_g}{\tau_o c_{ts}}$ scales with c in our tests. Mesh resolution can also affect the values of L and Δt . It has been pointed out in [13,38] that scaling using the value of Δl_z , the grid spacing along the slip plane normal direction, is required when $\Delta l_z > d^a$. Our calibration is valid for a non-orthogonal BCC grid with a grid spacing of $b:b:b$. And as a consequence of using this grid, our $\Delta l_z = d$. With a different mesh resolution, a re-calibration will be necessary, especially when $\Delta l_z > d$.

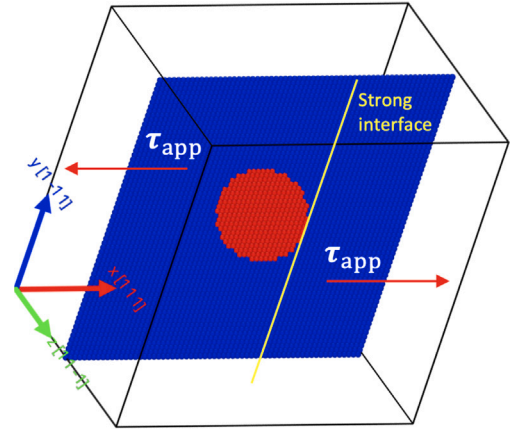


Fig. 5. Simulation setup for loop transmission through a strong interface.

4. Results and discussion

4.1. Dislocation transmission across a strong interface

To test the KMC routine, we simulated the interaction of an expanding dislocation loop in W with a strong interface that will only let the dislocation transmit using the KMC routine, i.e. thermal activation is needed for transmission as the mechanical energy from the applied stress is not sufficient. We assigned representative values for $\Delta H = 0.1$ eV and $v_{\text{eff}} = 10^{13}$ that reflect a strong interface. These values can also be informed with a lower scale model as we did for a grain boundary in Section 4.2. Finally, we note that the simulation results presented in this section utilized a transition function of $\beta(\theta) = 1$, so that the mobility of edge, screw, and mixed-type dislocations are the same. The set-up is shown in Fig. 5. $\tau_{\text{app}} = 0.245 \mu$ is the resolved shear stress. The BCC, non-orthogonal computational grid was used and the size was $64b \times 64b \times 64b$. All simulations utilized periodic boundary conditions. The test was repeated for different temperatures ($T = 300$ K, 400 K, 500 K, 600 K) and varying seeds required by the random number generator in the KMC routine.

The effect of varying temperature on the dislocation loop transmission behavior is shown in Fig. 6. The colored grid points correspond to the part of loop that met the interface and triggered the KMC routine. This segment increases in length as the loop continues to expand and more and more points impinge upon the interface. Each point triggers the KMC routine, shown as colored points in Fig. 6. The colors show the

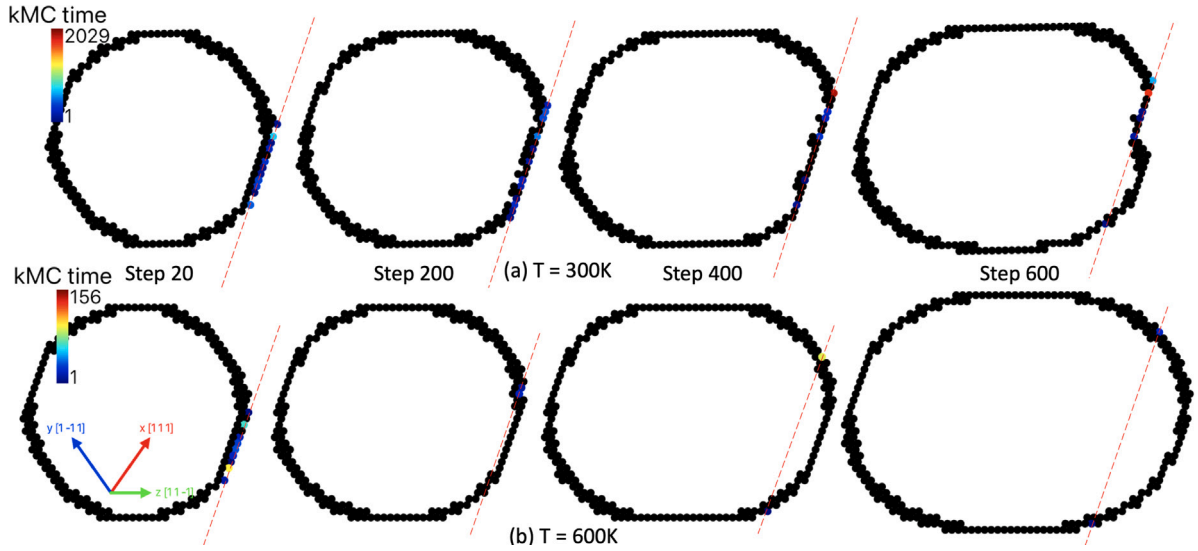


Fig. 6. Snapshots of loop transmission through a strong interface by the KMC routine at (a) 300 K and (b) 600 K. The loop is represented using the grid points selected as the dislocation center and colored with their normalized KMC time.

normalized KMC time ($\Delta t_k / \Delta t$) for that point, and each point represents a short (defined by the grid spacing) dislocation segment. Red points indicate longer wait times, and as the simulation evolves, the remaining wait time will count down, changing the color at a point from red to yellow to blue, which then indicates that transmission is imminent.

Fig. 6 clearly shows the temperature dependence in the transmission behavior of the dislocation, with transmission occurring earlier at higher temperatures as one might expect. For example, at Step 400, the loop at $T = 300$ K is still at the interface while the loop at $T = 600$ K shows a significant portion of the loop has already transmitted. The difference in time scales can also be seen in the magnitudes of the normalized KMC times. In the $T = 300$ K case, red points (or segments with the longest wait time) will wait an order of magnitude longer than the analogous points in the $T = 600$ K case.

Fig. 7 presents results from simulations using different seeds for the random number generator in the KMC routine (see Eq. (3.1)). The temperature was set at 500 K for both simulations. Since only the random seeds have changed, we would expect the transmission behavior to essentially be the same, with only statistical variations. The results clearly demonstrate this. The maximum normalized KMC times are 185 and 281, which are very similar. As a result, the two loops expand and transmit around the same time step (between Step 200 and 400); however some slight differences in the nature of transmission can be seen. For example, in Fig. 7(a) at Step 200, the loop has just transmitted across the interface, while the loop in Fig. 7(b) is still pinned. Thus, at Step 400, the loop in Fig. 7(a) has progressed past the interface slightly further than the loop in Fig. 7(b) at the same time step. In this case, transmission activity over a substantial portion of the loop is still observed, and the loop shape is very similar in both cases shown in Fig. 7.

As a property of the exponential distribution, the average KMC time generated with Eq. (3.1) should satisfy: $\overline{\Delta t_k} = \frac{1}{\Gamma_k}$. Therefore, for this simulation, we should obtain:

$$\ln\left(\frac{\overline{\Delta t_k}}{\Delta t}\right) = \frac{\Delta H}{\kappa_b T} + \ln\left(\frac{1}{v_{\text{eff}} \Delta t}\right) = \frac{0.1}{\kappa_b T} + 1.726 \quad (4.1)$$

We calculated the average normalized KMC time $\overline{\frac{\Delta t_k}{\Delta t}}$ for each temperature and plotted the results in Fig. 8. The interpolation gives: $\ln\left(\frac{\overline{\Delta t_k}}{\Delta t}\right) = \frac{0.1025}{\kappa_b T} + 1.7274$, which matches remarkably well with Eq. (4.1) and thus validates our implementation.

4.2. Dislocation transmission across a grain boundary

To demonstrate the applicability of the KMC-PFDD model for a more realistic case, we model dislocation transmission across a grain boundary (GB) in W. We chose to study the interaction of a $\Sigma 3 < 110 > \{112\}$ symmetric tilt GB (mis-orientation angle of 70.52°) with a mixed dislocation oriented at 70.55° to the $\langle 111 \rangle$ Burgers vector. The activation energies and pre-factors required for this study were calculated using molecular dynamics (MD) simulations. In MD, the initial GB structure was created using the method described in Ref. [42] and had an excess energy of 640 mJ/m^2 after energy minimization. The simulation cell has dimensions of approximately 2.196, 102.274, and 53.799 nm in the X, Y, and Z directions and contained 758400 atoms. A dipole of mixed dislocations was inserted into one of the grains of the simulation cell using ATOMSK software [43], with the line oriented along X. The dislocations were driven to the GB by applying a resolved shear stress of 1.6 GPa in the NPT ensemble for 100 ps. Following this, simulations were performed in the NVT ensemble for 3 ns and the event time was calculated as the time at which either of the dislocations in the dipole were found to transmit across the GB. The NVT runs were performed using a Langevin thermostat with a damping value of 1.0 ps. Independent trials were performed by changing the random number seeds for both the initial velocity distribution and the Langevin thermostat. We saw that in some cases the dislocations would transmit across the GB during the NPT run and these trials were discarded. Average rates for dislocation transmission were calculated at temperatures of 1500 K, 1525 K, 1550 K, 1575 K, 1600 K, and 1625 K using 10 independent trials and are shown in Fig. 9. These rates were used to predict the normalized activation energy (0.7555 eV/nm) and the pre-factor ($6.339 \times 10^{14} \text{ s}^{-1}$). A timestep of 1 fs was used in all MD simulations.

In the KMC-PFDD simulations most of the simulation set-up parameters were kept the same as in Section 4.1. However, in this set-up two GBs were placed along two sides of the dislocation loop (along x direction) since the KMC time in this case would be much larger compared to the strong interface case. In the absence of two GBs, segments of the loop can propagate and interact with their periodic images. As the event time for each dislocation segment that interacts with the GB in PFDD is sampled independently, we calculated the effective activation energy as the product of the normalized activation energy and the segment length in PFDD (b). This results in an activation energy of 0.2054 eV for a segment of length b.

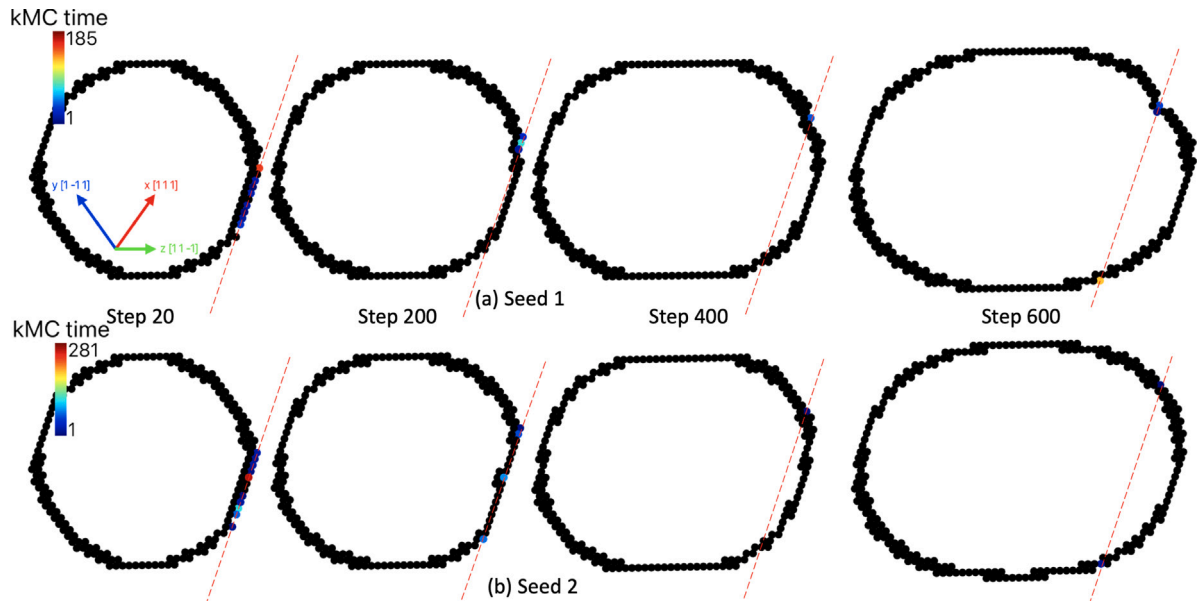


Fig. 7. Snapshots of loop transmission through a strong interface with (a) Seed 1 and (b) Seed 2. The loop is represented using the grid points selected as the dislocation center and colored with their normalized KMC time.

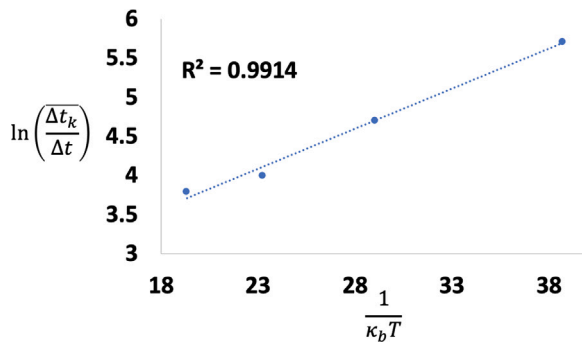


Fig. 8. Average KMC time as a function of temperature.

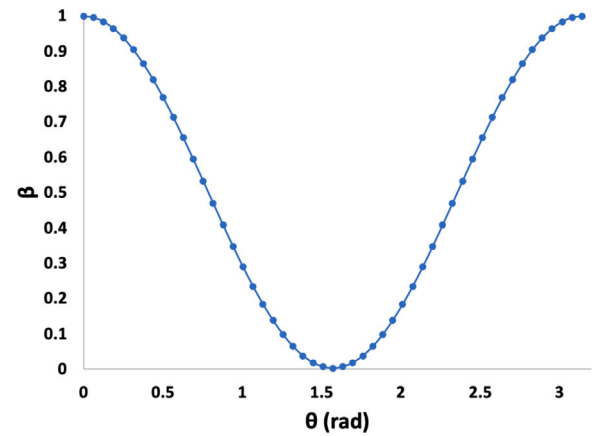


Fig. 10. Transition function used within the lattice energy to account for the difference in edge, screw and mixed-typed dislocation mobility in W.

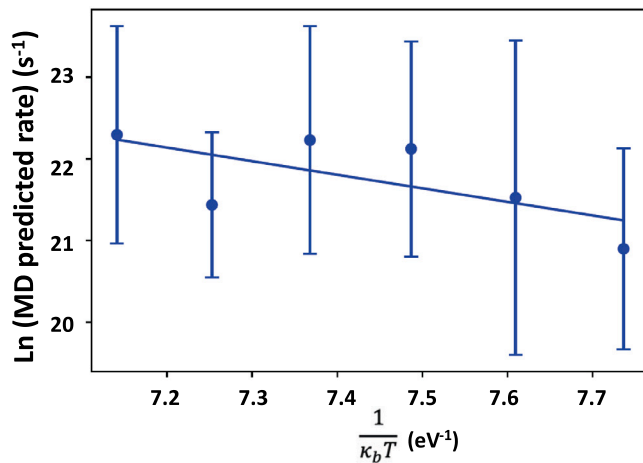


Fig. 9. Average MD-predicted rates for transmission of a mixed dislocation across a $\Sigma 3<110>\{112\}$ symmetric tilt GB. The error bars represent one standard deviation of the mean.

In addition, for the more realistic case, a line-character-dependent lattice energy was used to better model the difference in the lattice friction for the screw and edge segments. The transition function shown

in Eq. (2.6) was utilized with $R = 326.7$ for W, which was determined with the EAM3 potential [44]. With this parameterization, the form of the transition function, $\beta(\theta)$ is shown in Fig. 10. We note that while this case is more realistic than the strong interface case discussed previously, the GB in this simulation does not include any structure, such as a misfit dislocation structure. Again, the dislocation can only transmit through the GB if allowed by the KMC algorithm.

We performed this simulation with two different random number seeds, denoted as seed 3 and seed 4 respectively, and at $T = 300$ K. Hence, the maximum normalized KMC times in these two cases are both around 1000. The snapshots of the loop transmission event are shown in Figs. 11 and 12. A black-white color scheme is used for the order parameter ζ and yellow is used for grid points selected as the dislocation center. Those grid points with an active KMC time were colored according to their KMC time.

Compared to the strong interface case tested previously, this case shows a lot more variation in the transmitting dislocation segments. Rather than a large segment of the loop bowing into the material on the other side of the interface, these more realistic cases show narrow “fingers”, which are relatively small segments bowing out and extending across the interface. This transmission mechanisms prevails for both

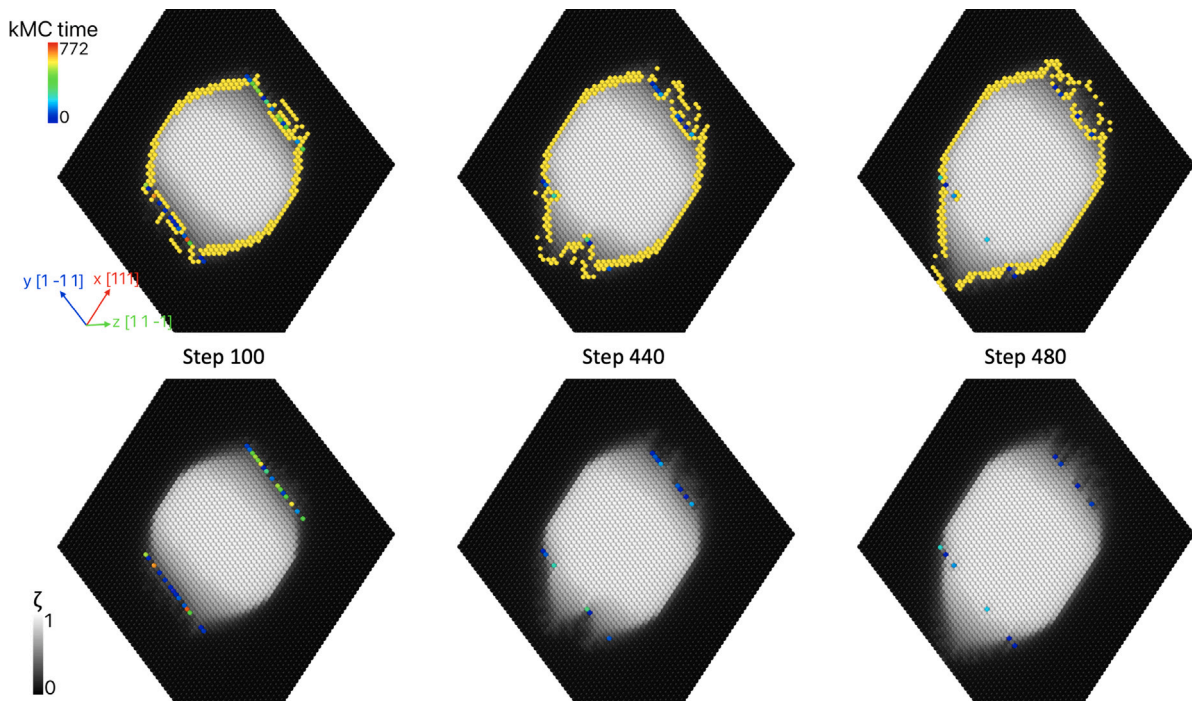


Fig. 11. Snapshots of loop transmission through a grain boundary by the KMC routine with seed 3. In the top row, the grid points were colored with their KMC time and the dislocation center was colored in yellow. In the bottom row, the grid points were colored with the order parameter value ζ .

interfaces modeled. The transmission proceeds until either several of these fingers coalesce or a fairly large segment of the dislocation held back at the interface is permitted to transmit. Once either event occurs, a much longer dislocation segment bows out, signifying significant slip transmission.

In cases where the order parameter no longer evolves at a grid point but having transmitted, continues to evolve at neighboring grid points, it is possible to have no or a multiple number of inflection points. Thus, the algorithm that identifies inflection point in the order parameter may miss or find extra points for the dislocation center, and in these cases the yellow points appear discontinuous. While this could likely be improved with a finer grid spacing, previous work in which the grid spacing was varied showed that the physical grid spacing produces the best comparison to atomistic results [45]. We note that despite the discontinuity in the dislocation center region, the bottom row of Figs. 11 and 12 clearly show that the order parameter field is still continuous. Also, once the dislocation clearly shows bow-out across the interface, the dislocation center becomes continuous once again (e.g., at the lower interface in Fig. 11, Step 480, and at the upper interface in Fig. 12).

The likely reason these extended fingers (or smaller bow-out regions) appear in these simulations and not in the previous strong interface case is that the KMC time is larger (by one order of magnitude). Thus, the variation in calculated KMC times at each point along the interface will also be much larger. This makes it more likely that a segment that has to wait a fairly long time will be next to a segment that has to wait a fairly short time. The segments waiting short times are allowed to transmit across the interface earlier, resulting in many small bowed-out segments.

In one case, we see a large portion of the dislocation bow-out into the neighboring material, and continue to grow. This behavior is more like that seen in the strong interface case shown in the previous section. An example of this can be seen at the lower interface in Fig. 11. At Step 440, dislocation bow-out is clear as it first attempts to transmit. In later time steps, this piece continues to grow and the neighboring segments along the interface subsequently follow. In this case the transmission event occurred slightly earlier across the lower GB in comparison to

transmission events for the other realization (random number seed) tested (Fig. 12). This is because a relatively large segment of the loop at the lower interface had a relatively small KMC time, and it was permitted to bow-out, while other segments at the other interface still had much more time left to wait before the transmission was allowed. This also illustrates the greater statistical variation between these two more realistic cases (Figs. 11 and 12) than the strong interface case (Fig. 7) due to the longer KMC times.

In cases where the fingers bow-out and coalesce on the other side of the interface, some of the segments waiting a long time may get “stuck” waiting at the interface, while the rest of the loop continues to bow-out on the other side of the interface. An example of this can be seen at the upper interface in Fig. 11 and lower interface in Fig. 12 at Step 480. The points remaining at the interface will stay waiting until the KMC algorithm allows them to evolve. This creates a small region (one or two points long) in which the order parameter is a non-integer value surrounded by region that has fully slipped (i.e., the order parameter has an integer value greater than the values at the points remaining at the interface). In PFDD this is representative of a very small fractional dislocation loop, and once the points at the interface are allowed to evolve this loop will collapse and vanish. These simulations cannot determine whether such behavior is physical or not since the interface structure is not accounted for. Moreover, changes in the local stress state, due to transmission of dislocation segments, will result in changes in the activation energy barrier for neighboring segments. Presumably, in this case, the finger-like morphology seen in the current simulations would either be diminished to some extent or possibly not be present at all. To include local stress effects, the local stress state would need to be calculated on-the-fly, and when significant changes are detected, the wait times would need to be resampled or recalculated. Thus, wait times at relevant neighboring points would be updated using the local stress state in Eq. (3.3) rather than a global stress state. While this is an important effect to consider when modeling dislocation-interface interactions, such an extension will be left for future work. Our current aim is to demonstrate the integration of a KMC scheme within the PFDD method to model thermally activated dislocation motion. However, this is only one step towards achieving a KMC-PFDD model that can fully capture thermally activated dislocation-interface interactions.

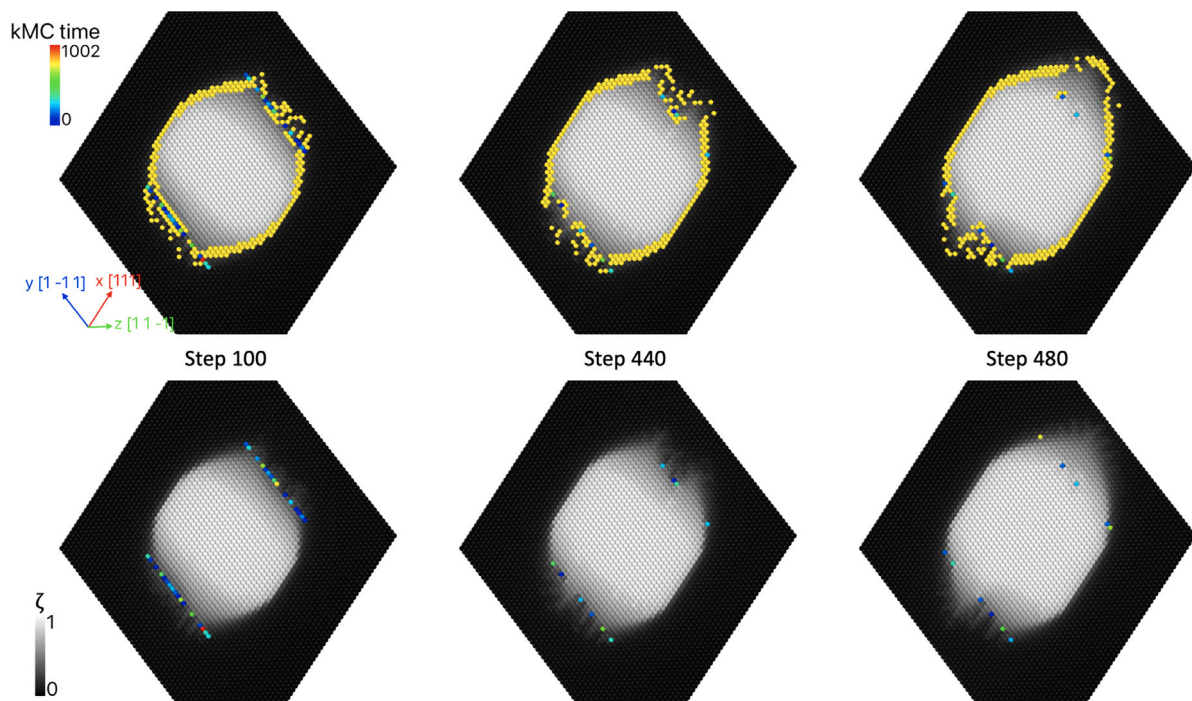


Fig. 12. Snapshots of loop transmission through a grain boundary by the KMC routine with seed 4. In the top row, the grid points were colored with their KMC time and the dislocation center was colored in yellow. In the bottom row, the grid points were colored with the order parameter value ζ .

As another example, in Fig. 12 the loop requires slightly more time to show significant bow-out than the loop in Fig. 11, and ultimately shows transmission at both the interfaces, whereas the loop in Fig. 11 only shows transmission at the lower interface at these timescales.

Finally, we see that sections of the loop that are not in line with the GBs do not propagate and annihilate with their periodic images. This occurs because of the use of the line-character dependent lattice energy Eq. (2.6). The screw segment has a higher energy barrier than the edge and thus remains mostly stationary. We note that this also indicates that the dislocation is not in a free glide regime, and that thermal activation is important for dislocation motion in the simulated situation (the KMC-PFDD algorithm does not account for thermal dependence of the drag coefficient [39,46]).

5. Conclusions

In this paper, we have presented a combined kinetic Monte Carlo (KMC) - Phase Field Dislocation Dynamics (PFDD) approach designed to model thermally activated dislocation behavior in metals and alloys. In addition to integrating Gillespie's Stochastic Simulation algorithm into the original PFDD algorithm, additional algorithmic enhancements were required, such as identification and on-the-fly tracking of the center of the dislocation, which was achieved through calculation of inflection points in the order parameter fields. The new algorithm is tested for two cases: (1) a strong interface, and (2) a more realistic GB case. In the latter case, the interaction of a $\Sigma 3(110)\{112\}$ symmetric tilt GB in W with a mixed dislocation oriented at 70.55° to the $\langle 111 \rangle$ Burgers vector was modeled, and necessary information such as the activation energy was provided from MD simulations. This simulation utilized a non-orthogonal computational grid, which aligned computational points with the BCC structure of W, and a transition function to account for character-dependent dislocation mobility. The results show expected trends for thermally activated transmission of dislocation across an interface. Specifically, at higher temperatures, slip transfer occurs at higher rates than in simulations at lower temperatures. Statistical variations between independent trials are evident in the transmission process, especially with realistic rate coefficients. The

proposed KMC-PFDD framework is general and can be applied to model thermally activated processes in dislocation-mediated plasticity with rate coefficients inferred from atomic-scale simulations or experiments.

CRediT authorship contribution statement

Xiaoyao Peng: Conceptualization, Methodology, Software, Validation, Writing – original draft, Visualization. **Nithin Mathew:** Conceptualization, Methodology, Validation, Writing – original draft. **Irene J. Beyerlein:** Conceptualization, Methodology, Writing – review & editing. **Enrique Martinez:** Conceptualization, Methodology, Software, Writing – review & editing. **Abigail Hunter:** Conceptualization, Methodology, Writing – original draft, Project administration, Funding acquisition.

Declaration of competing interest

The authors declare that they have no known competing financial interests or personal relationships that could have appeared to influence the work reported in this paper.

Data availability

Data will be made available on request.

Acknowledgments

XP, AH and NM gratefully acknowledge support from the Laboratory Directed Research and Development (LDRD), United States of America Program through project 20210036DR at Los Alamos National Laboratory (LANL). XP and AH also acknowledge support from the Institute of Materials Science at LANL, United States of America. IJB gratefully acknowledges support from the Office of Naval Research, United States under contract N00014-21-1-2536. EMS acknowledges support by the National Science Foundation EPSCoR Program under NSF, United States of America Award OIA-1655740.

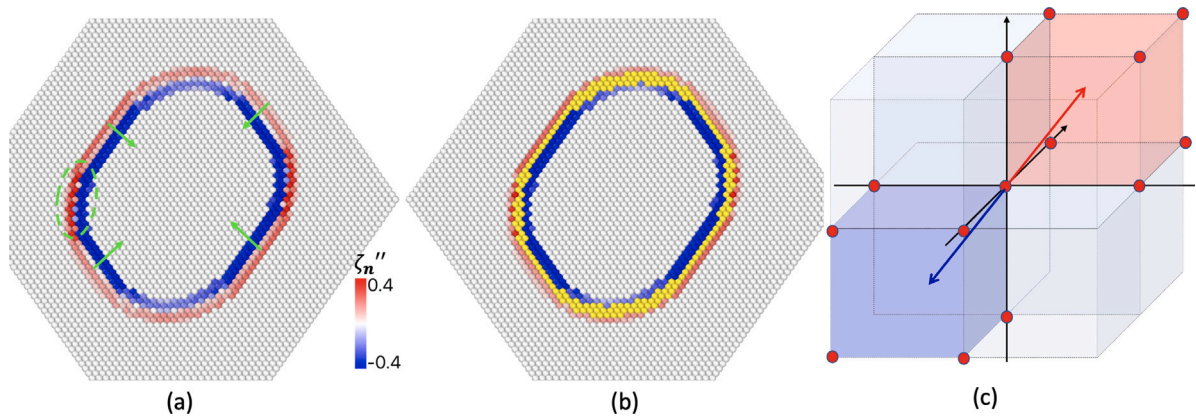


Fig. A.1. (a) A dislocation loop colored with the value of ζ_n'' . Green arrows indicate the gradient direction \mathbf{n} . (b) The selected grid points as the dislocation center are marked in yellow. (c) Two octants at the positive and negative gradient directions respectively. Vertex points used for the averaging are shown as red circles.

Appendix

In Section 3.2, we gave two conditions, Eqs. (3.6) and (3.7), to select grid points as the dislocation center. In this appendix, we provide details of how they are executed in the simulations. Fig. A.1(a) shows a dislocation loop colored with the value of $\zeta_n''(\mathbf{X})$. The primary goal of the algorithm is to select the inflection point along the gradient direction, which is indicated with the green arrows around the loop. The two conditions, Eqs. (3.6) and (3.7), indicate that a selected inflection point, $\mathbf{X}(i, j, k)$, should have $\zeta_n''(\mathbf{X}(i, j, k)) \approx 0$ (white in color) and a neighboring point in the positive gradient direction $\zeta_n''(\mathbf{X}(i + \Delta i, j + \Delta j, k + \Delta k)) < 0$ (blue in color) and a neighboring point in the negative gradient direction $\zeta_n''(\mathbf{X}(i - \Delta i, j - \Delta j, k - \Delta k)) > 0$ (red in color), with $\Delta i, \Delta j, \Delta k = 0$ or ± 1 . However, depending on how wide the core region is, it is not guaranteed that a white inflection point exists surrounded by a blue and red points. For example, in Fig. A.1(a), the region circled by a dashed green line, where there are mixed type dislocation character, does not have points in white or close to white. So we need to pick the closest point to an inflection point. This is done by taking an average of ζ_n'' over the eight vertex points of the octant along the positive and negative directions. In Fig. A.1(c), two octants at the positive (blue) and negative (red) gradient directions are shown. If $\frac{1}{8} \sum_{v=1}^8 \zeta_n''(\mathbf{X}_{\text{pos}}(v)) < 0$ and $\frac{1}{8} \sum_{v=1}^8 \zeta_n''(\mathbf{X}_{\text{neg}}(v)) > 0$ then $\mathbf{X}(i, j, k)$ is selected. Fig. A.1(b) shows all points selected for this dislocation loop in yellow.

References

- [1] Masato Hiratani, Hussein M. Zbib, Stochastic dislocation dynamics for dislocation-defects interaction: A multiscale modeling approach, *J. Eng. Mater. Technol.* 124 (3) (2002) 335–341.
- [2] M. Hiratani, H.M. Zbib, On dislocation–defect interactions and patterning: stochastic discrete dislocation dynamics (SDD), *J. Nucl. Mater.* 323 (2) (2003) 290–303, Proceedings of the Second IEA Fusion Materials Agreement Workshop on Modeling and Experimental Validation.
- [3] Yang Li, Max Boleininger, Christian Robertson, Laurent Dupuy, Sergei L. Dudarev, Diffusion and interaction of prismatic dislocation loops simulated by stochastic discrete dislocation dynamics, *Phys. Rev. Mater.* 3 (2019) 073805.
- [4] Wei Cai, Vasily V. Bulatov, Sidney Yip, Ali S. Argon, Kinetic Monte Carlo modeling of dislocation motion in BCC metals, *Mater. Sci. Eng. A* 309–310 (2001) 270–273, Dislocations 2000: An International Conference on the Fundamentals of Plastic Deformation.
- [5] Wei Cai, Vasily V. Bulatov, João F. Justo, Ali S. Argon, Sidney Yip, Kinetic Monte Carlo approach to modeling dislocation mobility, *Comput. Mater. Sci.* 23 (1) (2002) 124–130.
- [6] Alexander Stukowski, David Cereceda, Thomas D. Swinburne, Jaime Marian, Thermally-activated non-Schmid glide of screw dislocations in W using atomistically-informed kinetic Monte Carlo simulations, *Int. J. Plast.* 65 (2015) 108–130.
- [7] M. Prieto-Depedro, I. Martin-Bragado, J. Segurado, An atomistically informed kinetic Monte Carlo model of grain boundary motion coupled to shear deformation, *Int. J. Plast.* 68 (2015) 98–110.
- [8] Chaitanya S. Deo, David J. Srolovitz, Wei Cai, Vasily V. Bulatov, Kinetic Monte Carlo method for dislocation migration in the presence of solute, *Phys. Rev. B* 71 (2005) 014106.
- [9] C.S. Deo, D.J. Srolovitz, W. Cai, V.V. Bulatov, Stochastic simulation of dislocation glide in tantalum and Ta-based alloys, *J. Mech. Phys. Solids* 53 (6) (2005) 1223–1247.
- [10] Yue Zhao, Jaime Marian, Direct prediction of the solute softening-to-hardening transition in W–Re alloys using stochastic simulations of screw dislocation motion, *Modelling Simul. Mater. Sci. Eng.* 26 (4) (2018) 045002.
- [11] Shuhei Shinzato, Masato Wakeda, Shigenobu Ogata, An atomistically informed kinetic Monte Carlo model for predicting solid solution strengthening of body-centered cubic alloys, *Int. J. Plast.* 122 (2019) 319–337.
- [12] Marisol Koslowski, Alberto M. Cuitino, Michael Ortiz, A phase-field theory of dislocation dynamics, strain hardening and hysteresis in ductile single crystals, *J. Mech. Phys. Solids* 50 (12) (2002) 2597–2635.
- [13] Yu U. Wang, Y.M. Jin, A.M. Cuitino, A.G. Khachaturyan, Nanoscale phase field microelasticity theory of dislocations: model and 3D simulations, *Acta Mater.* 49 (10) (2001) 1847–1857.
- [14] Jaber Rezaei Mianroodi, Bob Svendsen, Atomistically determined phase-field modeling of dislocation dissociation, stacking fault formation, dislocation slip, and reactions in fcc systems, *J. Mech. Phys. Solids* 77 (2015) 109–122.
- [15] Abigail Hunter, Irene J. Beyerlein, Timothy C. Germann, Marisol Koslowski, Influence of the stacking fault energy surface on partial dislocations in fcc metals with a three-dimensional phase field dislocations dynamics model, *Phys. Rev. B* 84 (14) (2011) 144108.
- [16] Xiaoyao Peng, Nithin Mathew, Irene J. Beyerlein, Kaushik Dayal, Abigail Hunter, A 3D phase field dislocation dynamics model for body-centered cubic crystals, *Comput. Mater. Sci.* 171 (2020) 109217.
- [17] Hyojung Kim, Alexandra Zimmerman, Irene J. Beyerlein, Abigail Hunter, Phase field modeling of dislocations and obstacles in InSb, *J. Appl. Phys.* 132 (2) (2022) 025702.
- [18] Lauren T.W. Fey, Shuozhi Xu, Yanqing Su, Abigail Hunter, Irene J. Beyerlein, Transitions in the morphology and critical stresses of gliding dislocations in multiprincipal element alloys, *Phys. Rev. Mater.* 6 (1) (2022) 013605.
- [19] C. Albrecht, A. Hunter, A. Kumar, I.J. Beyerlein, A phase field model for dislocations in hexagonal close packed crystals, *J. Mech. Phys. Solids* 137 (2020) 103823.
- [20] Hong Liu, Yipeng Gao, Liang Qi, Yunzhi Wang, Jian-Feng Nie, Phase-field simulation of Orowan strengthening by coherent precipitate plates in an aluminum alloy, *Metall. Mater. Trans. A* 46 (7) (2015) 3287–3301.
- [21] Jaber Rezaei Mianroodi, Pratheek Shanthraj, Paraskevas Kontis, Jonathan Cormier, Baptiste Gault, Bob Svendsen, Dierk Raabe, Atomistic phase field chemomechanical modeling of dislocation-solute-precipitate interaction in Ni–Al–Co, *Acta Mater.* 175 (2019) 250–261.
- [22] Tengfei Ma, Hyojung Kim, Nithin Mathew, Darby J. Luscher, Lei Cao, Abigail Hunter, Dislocation transmission across $\sigma_3 \{111\}$ incoherent twin boundary: a combined atomistic and phase-field study, *Acta Mater.* 223 (2022) 117447.
- [23] Yifei Zeng, Abigail Hunter, Irene Jane Beyerlein, Marisol Koslowski, A phase field dislocation dynamics model for a bicrystal interface system: An investigation into dislocation slip transmission across cube-on-cube interfaces, *Int. J. Plast.* 79 (2016) 293–313.
- [24] S.Y. Hu, Y.L. Li, Y.X. Zheng, L.Q. Chen, Effect of solutes on dislocation motion—a phase-field simulation, *Int. J. Plast.* 20 (3) (2004) 403–425, Owen Richmond Memorial Special Issue.
- [25] C. Albrecht, I.J. Beyerlein, M.R. Jones, Temperature dependent phase field dislocation dynamics model, *Eur. J. Mech. A Solids* 100 (2023) 104987.

- [26] J.P. Simmons, Youhai Wen, C. Shen, Y.Z. Wang, Microstructural development involving nucleation and growth phenomena simulated with the Phase Field method, *Mater. Sci. Eng. A* 365 (1) (2004) 136–143, Multiscale Materials Modelling.
- [27] T.W. Heo, L.-Q. Chen, Phase-field modeling of nucleation in solid-state phase transformations, *JOM* 66 (2014) 1520–1528.
- [28] Jaber Rezaei Mianroodi, Abigail Hunter, Irene J. Beyerlein, Bob Svendsen, Theoretical and computational comparison of models for dislocation dissociation and stacking fault/core formation in fcc crystals, *J. Mech. Phys. Solids* 95 (2016) 719–741.
- [29] I.J. Beyerlein, A. Hunter, Understanding dislocation mechanics at the mesoscale using phase field dislocation dynamics, *Phil. Trans. R. Soc. A* 374 (2066) (2016) 20150166.
- [30] Shuozhi Xu, Lauren Smith, Jaber R. Mianroodi, Abigail Hunter, Bob Svendsen, Irene J. Beyerlein, A comparison of different continuum approaches in modeling mixed-type dislocations in Al, *Modelling Simul. Mater. Sci. Eng.* 27 (7) (2019) 074004.
- [31] Hyojung Kim, Nithin Mathew, Darby J. Luscher, Abigail Hunter, Phase field dislocation dynamics (PFDD) modeling of non-Schmid behavior in BCC metals informed by atomistic simulations, *J. Mech. Phys. Solids* 152 (2021) 104460.
- [32] Xiaoyao Peng, Abigail Hunter, Irene J. Beyerlein, Ricardo A. Lebensohn, Kaushik Dayal, Enrique Martinez, Non-orthogonal computational grids for studying dislocation motion in phase field approaches, *Comput. Mater. Sci.* 200 (2021) 110834.
- [33] Lauren T.W. Fey, Abigail Hunter, Irene J. Beyerlein, Phase-field dislocation modeling of cross-slip, *J. Mater. Sci.* (2022) 1–15.
- [34] Daniel T. Gillespie, A general method for numerically simulating the stochastic time evolution of coupled chemical reactions, *J. Comput. Phys.* 22 (4) (1976) 403–434.
- [35] G. Esteban-Manzanares, R. Santos-Güemes, I. Papadimitriou, E. Martínez, J. Llorca, Influence of the stress state on the cross-slip free energy barrier in Al: an atomistic investigation, *Acta Mater.* 184 (2020) 109–119.
- [36] A. Karma, W.-J. Rappel, Phase-field model of dendritic sidebranching with thermal noise, *Phys. Rev. E* 60 (4) (1999) 3614–3625.
- [37] Claire Albrecht, Anil Kumar, Shuozhi Xu, Abigail Hunter, Irene J. Beyerlein, Asymmetric equilibrium core structures of pyramidal-II < c+ a > dislocations in ten hexagonal-close-packed metals, *Phys. Rev. Mater.* 5 (4) (2021) 043602.
- [38] C. Shen, Y. Wang, Incorporation of γ -surface to phase field model of dislocations: simulating dislocation dissociation in fcc crystals, *Acta Mater.* 52 (3) (2004) 683–691.
- [39] Giacomo Po, Yinan Cui, David Rivera, David Cereceda, Tom D. Swinburne, Jaime Marian, Nasr Ghoniem, A phenomenological dislocation mobility law for bcc metals, *Acta Mater.* 119 (2016) 123–135.
- [40] Mihai-Cosmin Marinica, Lisa Ventelon, M.R. Gilbert, L. Proville, S.L. Dudarev, J. Marian, G. Bencteux, F. Willaime, Interatomic potentials for modelling radiation defects and dislocations in tungsten, *J. Phys.: Condens. Matter* 25 (39) (2013) 395502.
- [41] David Cereceda, Alexander Stukowski, M.R. Gilbert, Sylvain Queyreau, Lisa Ventelon, Mihai-Cosmin Marinica, J.M. Perlado, Jaime Marian, Assessment of interatomic potentials for atomistic analysis of static and dynamic properties of screw dislocations in W, *J. Phys.: Condens. Matter* 25 (8) (2013) 085702.
- [42] Mark A. Tschopp, Shawn P. Coleman, David L. McDowell, Symmetric and asymmetric tilt grain boundary structure and energy in Cu and Al (and transferability to other fcc metals), *Integr. Mater. Manuf. Innov.* 4 (1) (2015) 11.
- [43] Pierre Hirel, AtomsK: A tool for manipulating and converting atomic data files, *Comput. Phys. Comm.* 197 (2015) 212–219.
- [44] Giovanni Bonny, Dmitry Terentyev, Alexander Bakaev, Petr Grigorev, Dimitri Van Neck, Many-body central force potentials for tungsten, *Modelling Simul. Mater. Sci. Eng.* 22 (5) (2014) 053001.
- [45] Shuozhi Xu, Jaber R. Mianroodi, Abigail Hunter, Bob Svendsen, Irene J. Beyerlein, Comparative modeling of the disregistry and Peierls stress for dissociated edge and screw dislocations in Al, *Int. J. Plast.* 129 (2020) 102689.
- [46] Daniel N. Blaschke, Emil Mottola, Dean L. Preston, Dislocation drag from phonon wind in an isotropic crystal at large velocities, *Phil. Mag.* 100 (5) (2020) 571–600.